# Supplementary Materials

## Daily to centennial behavior of aseismic slip along the central section of the North Anatolian Fault

**R. Jolivet[1,2], J. Jara[1], M. Dalaison[1], B. Rouet-Leduc[3], A. Özdemir[4], U. Dogan[4], Z. Çakir[5], S. Ergintav[6]& P. Dubernet[1]**

[1]Laboratoire de Géologie, Département de Géosciences, École Normale Supérieure, PSL Université, CNRS UMR 8538, Paris, France

[2]Institut Universitaire de France, 1 rue Descartes, 75006 Paris

[3]Disaster Prevention Research Institute, Kyoto University, Kyoto, Japan

[4] Department of Geomatic Engineering, Yildiz Technical University, 34220 Istanbul, Turkey

[5]Department of Geology, Istanbul Technical University, 34469 Istanbul, Turkey

[6]Department of Geodesy, Kandilli Observatory and Earthquake Research Institute, Bogazici University, 34684 Istanbul, Turkey

Corresponding author: Romain Jolivet, romain.jolivet@ens.fr

# 1 InSAR data complementary figures

## 1.1 InSAR dataset

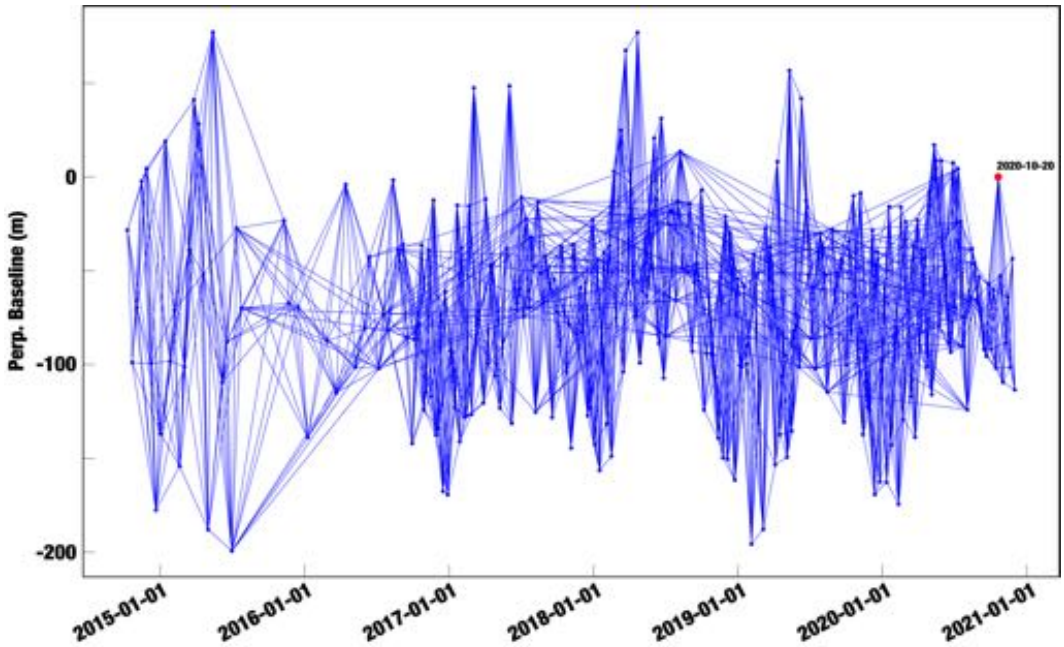


Figure S-1: **Perpendicular baseline as a function of acquisition dates for track 65 -** Blue dots represent the perpendicular baseline at the date of each acquisition by the Sentinel 1 A and B satellites. Red dot is the image chosen as reference for the geometry. Blue lines are the interferograms we computed.

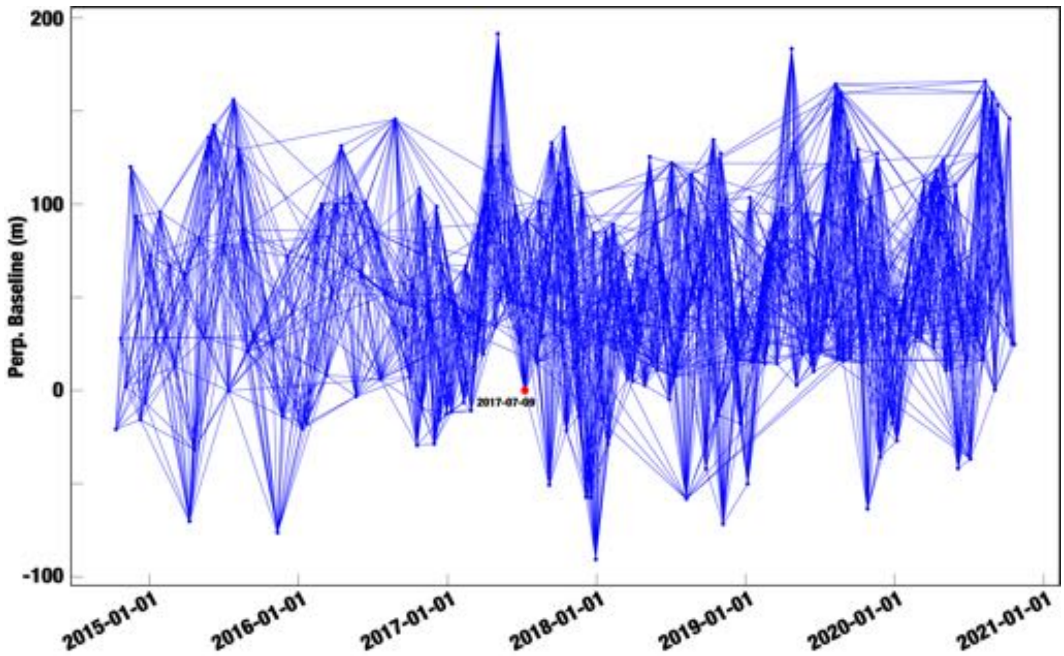


Figure S-2: **Perpendicular baseline as a function of acquisition dates for track 87 -** Blue dots represent the perpendicular baseline at the date of each acquisition by the Sentinel 1 A and B satellites. Red dot is the image chosen as reference for the geometry. Blue lines are the interferograms we computed.

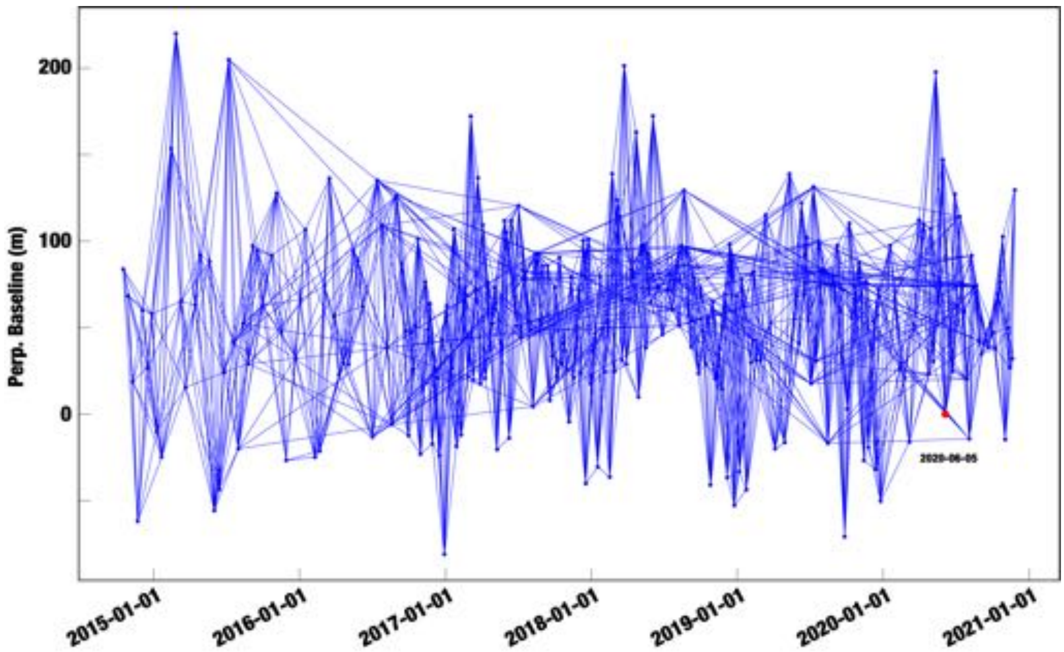


Figure S-3: **Perpendicular baseline as a function of acquisition dates for track 167-** Blue dots represent the perpendicular baseline at the date of each acquisition by the Sentinel 1 A and B satellites. Red dot is the image chosen as reference for the geometry. Blue lines are the interferograms we computed.

### 1.2 Full velocity maps

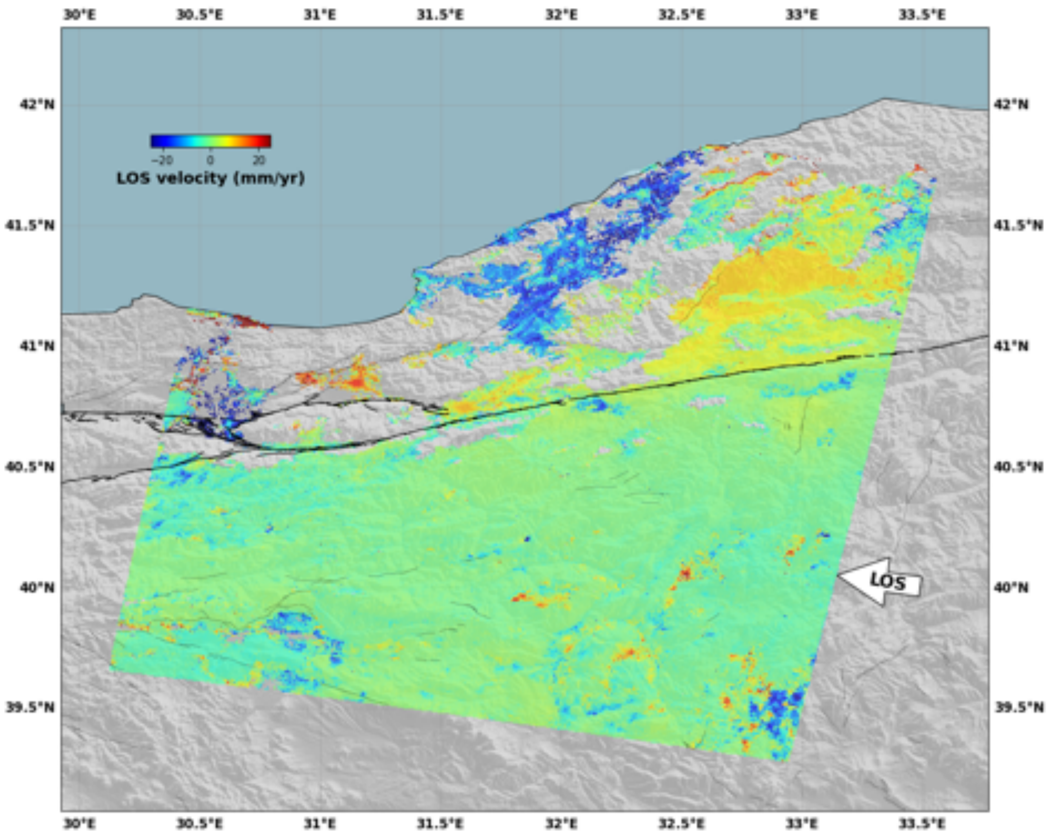


Figure S-4: **Line-of-sight velocity map from track 65 -** Velocity map computed from the time series of InSAR data on track 65. All available pixels are shown.

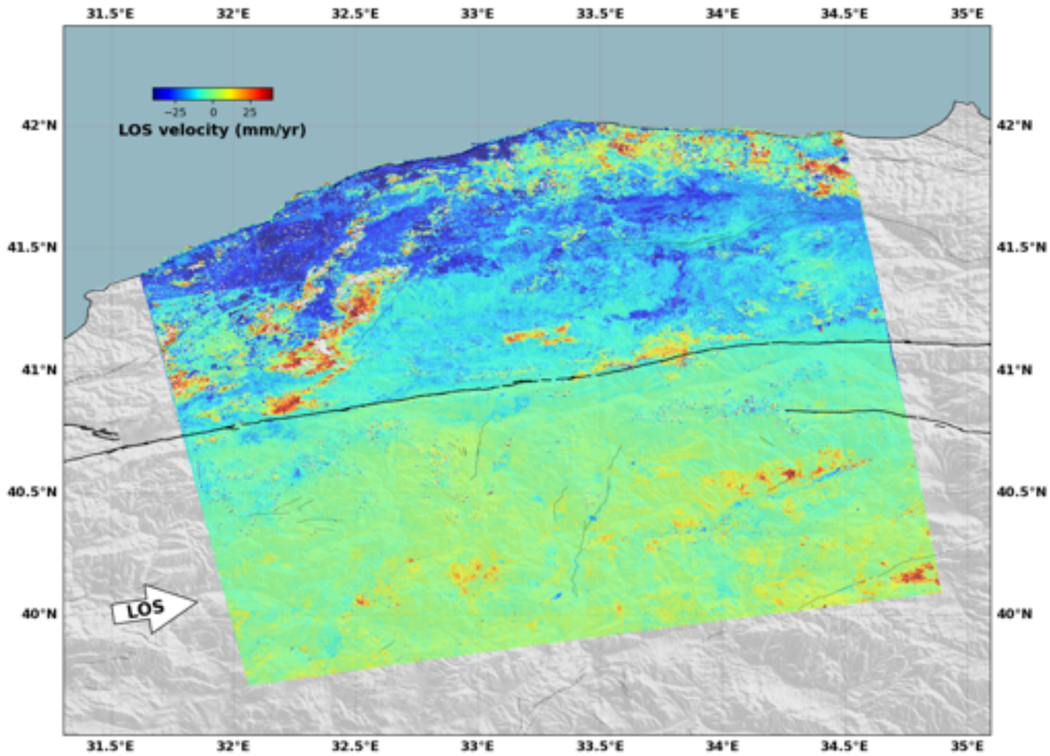


Figure S-5: **Line-of-sight velocity map from track 87 -** Velocity map computed from the time series of InSAR data on track 87. All available pixels are shown.

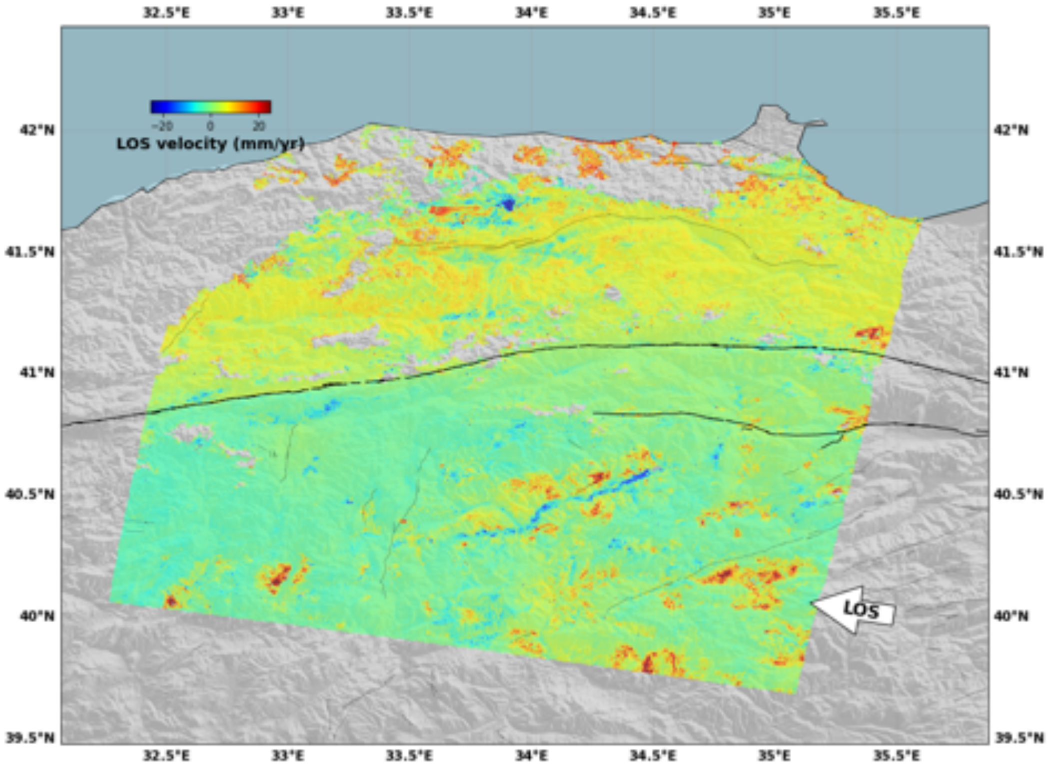


Figure S-6: **Line-of-sight velocity map from track 167 -** Velocity map computed from the time series of InSAR data on track 167. All available pixels are shown.

### 1.3 Velocity standard deviation maps

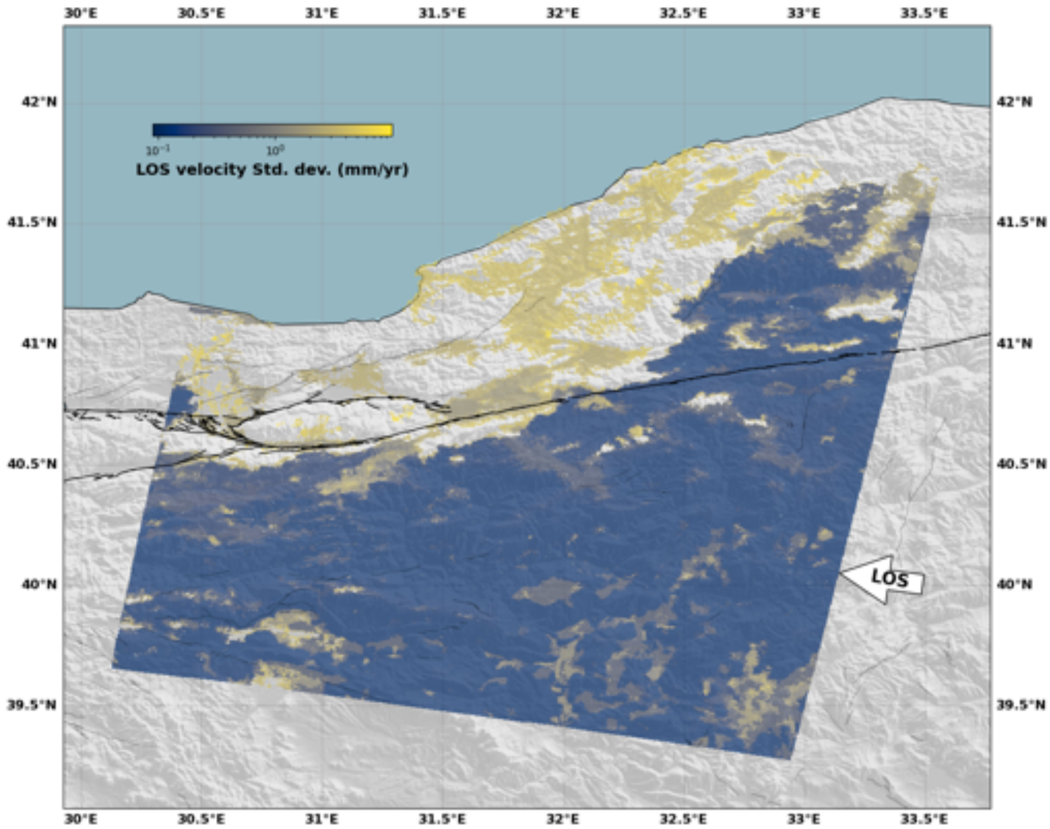


Figure S-7: **Line-of-sight velocity standard deviation map from track 65 -** Standard deviations are from the analyzed state covariance at the end of the Kalman filtering procedure.

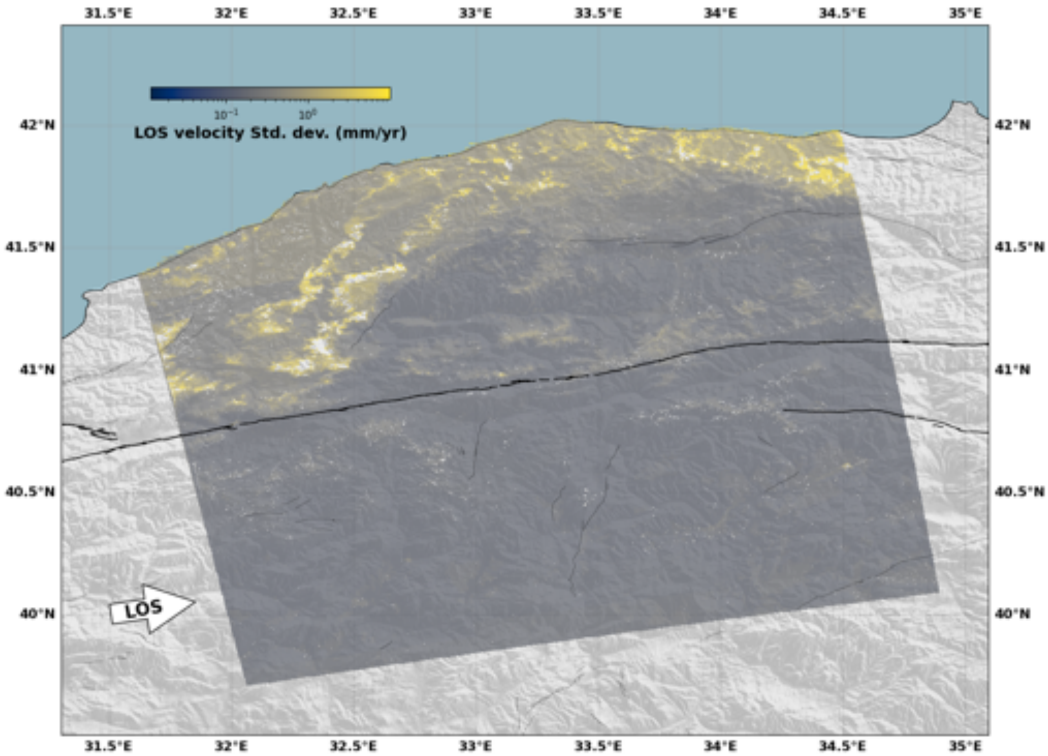


Figure S-8: **Line-of-sight velocity standard deviation map from track 87 -** Standard deviations are from the analyzed state covariance at the end of the Kalman filtering procedure.

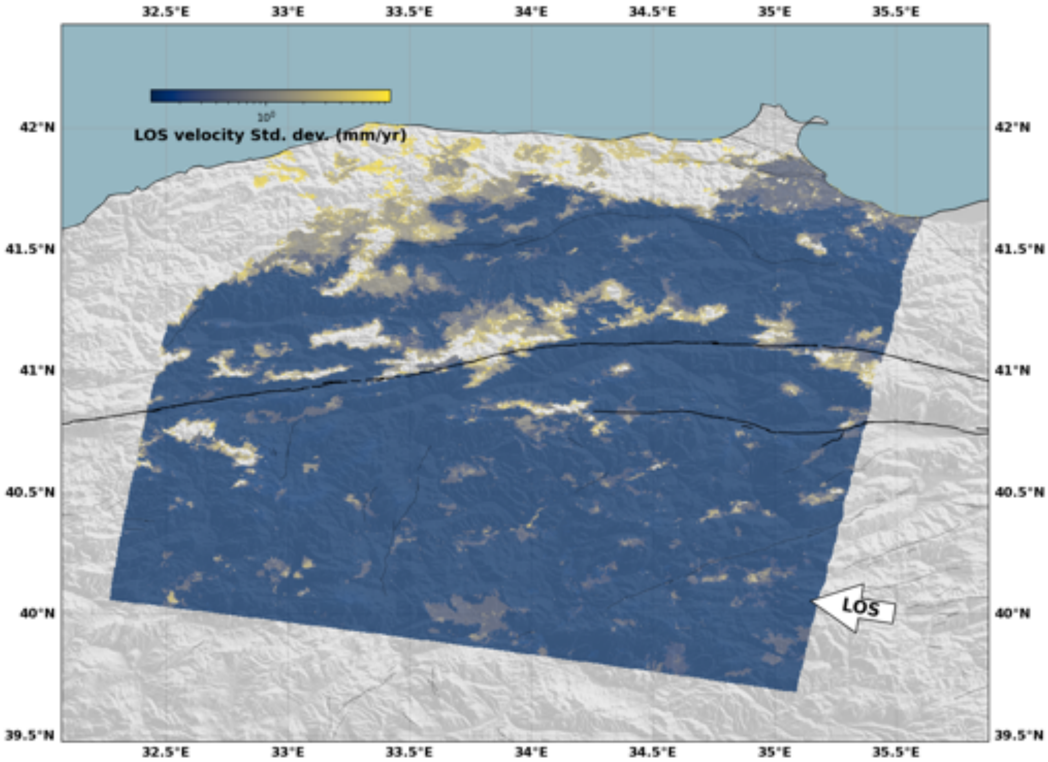


Figure S-9: **Line-of-sight velocity map standard deviation from track 167 -** Standard deviations are from the analyzed state covariance at the end of the Kalman filtering procedure.

### 1.4 Number of data per pixel

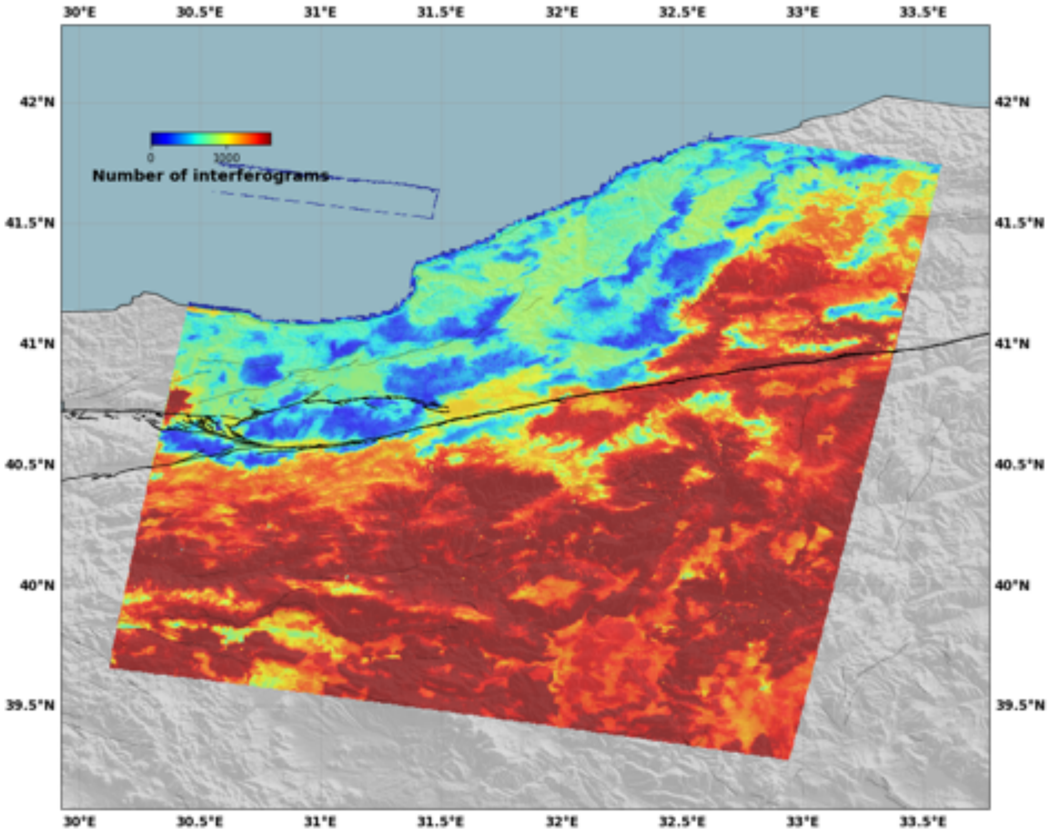


Figure S-10: **Number of interferograms available per pixels on track 65 -** Map of the number of unwrapped interferograms per pixel, used as one of the quality factor for pixel selection.

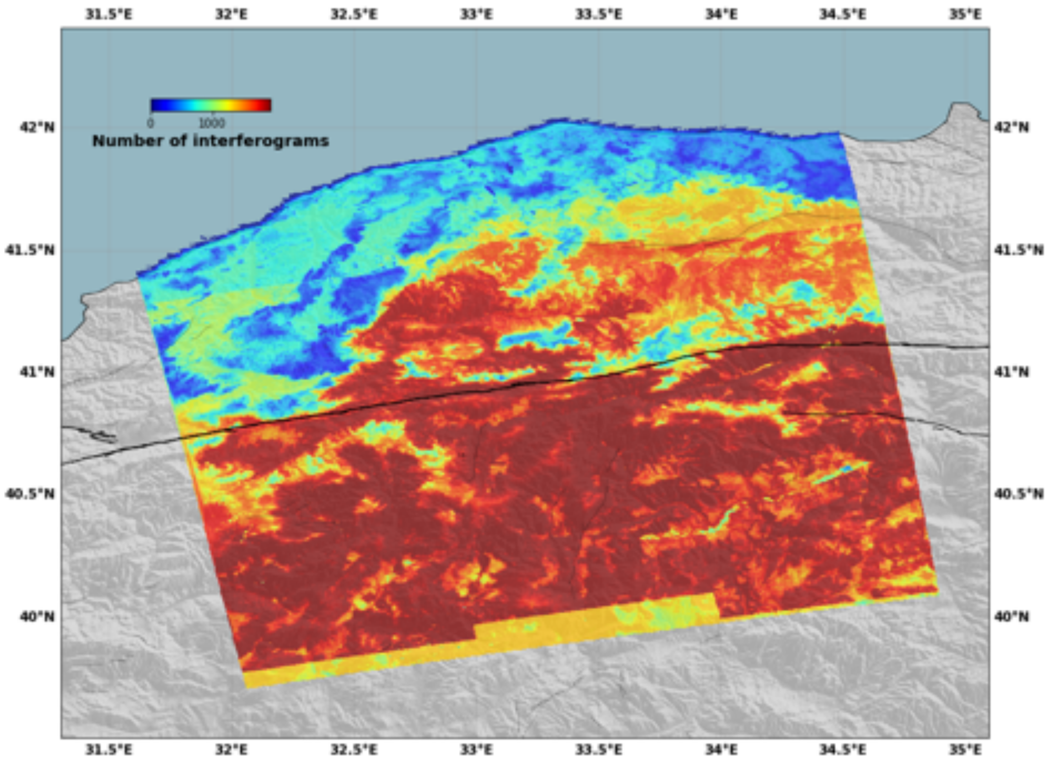


Figure S-11: **Number of interferograms available per pixels on track 87 -** Map of the number of unwrapped interferograms per pixel, used as one of the quality factor for pixel selection.

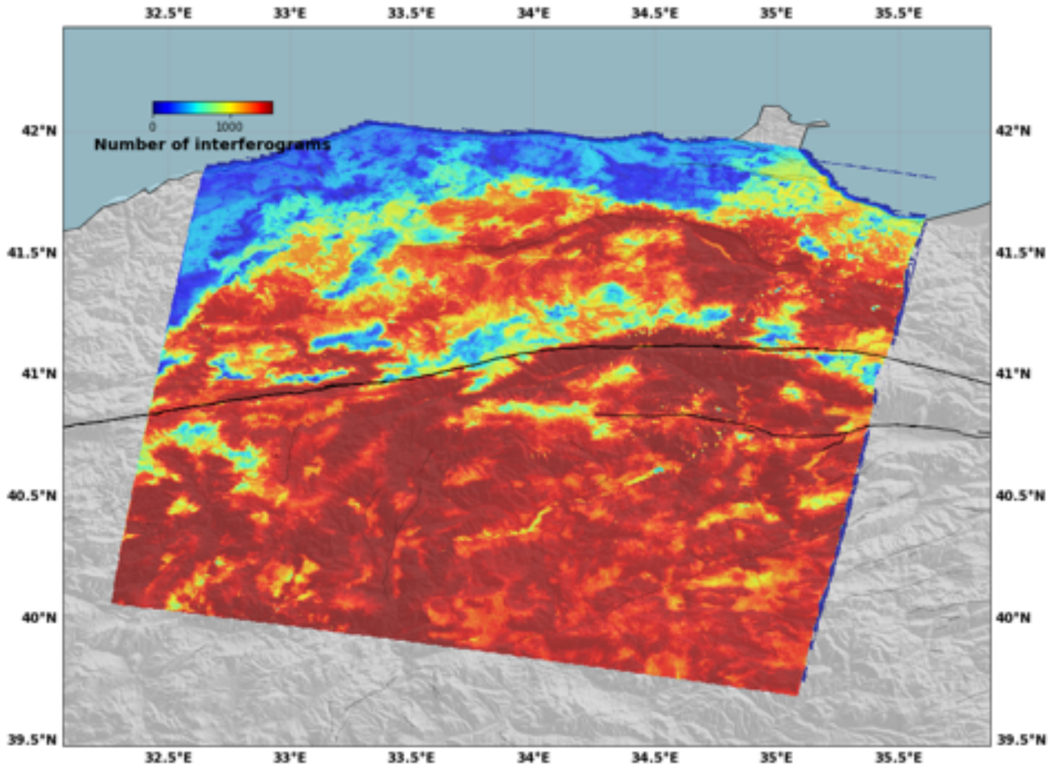


Figure S-12: **Number of interferograms available per pixels on 167 -** Map of the number of unwrapped interferograms per pixel, used as one of the quality factor for pixel selection.

### 1.5 RMS of time series reconstruction per pixel

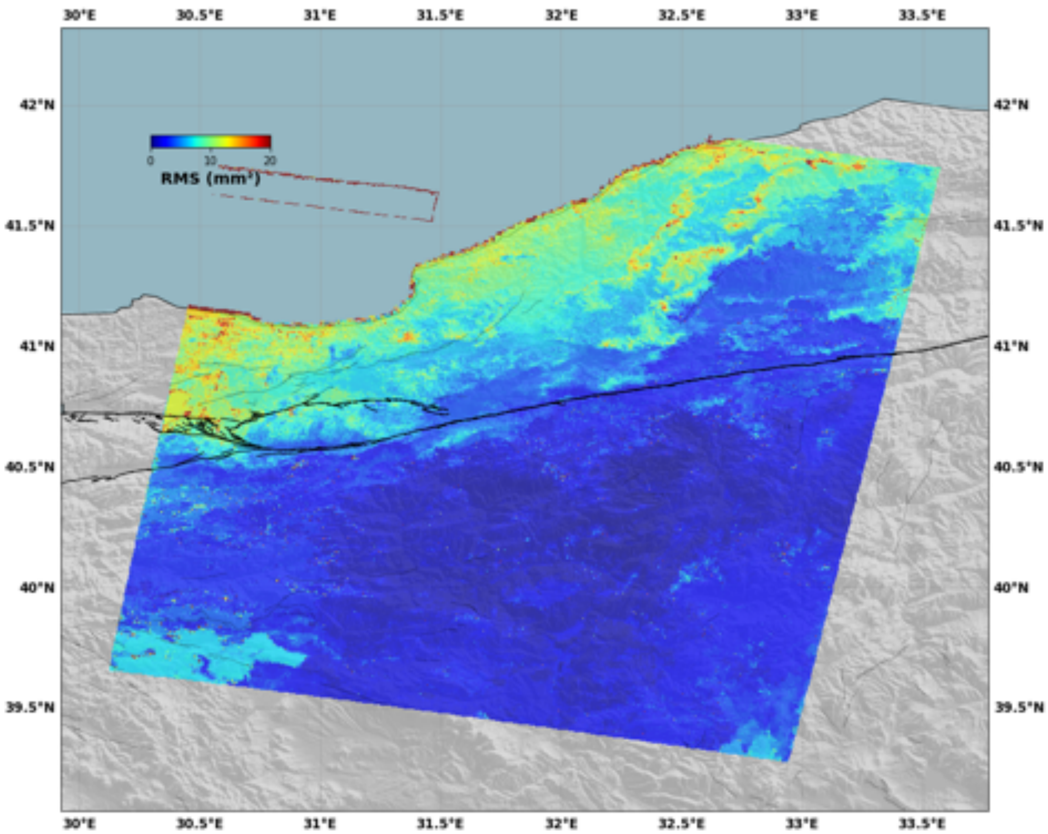


Figure S-13: **RMS of time series reconstruction for track 65 -** RMS is defined as the average of the square difference between data (i.e. interferograms) and time series reconstructions (i.e. interferograms predicted from the time series) and used as a quality factor for pixel selection.

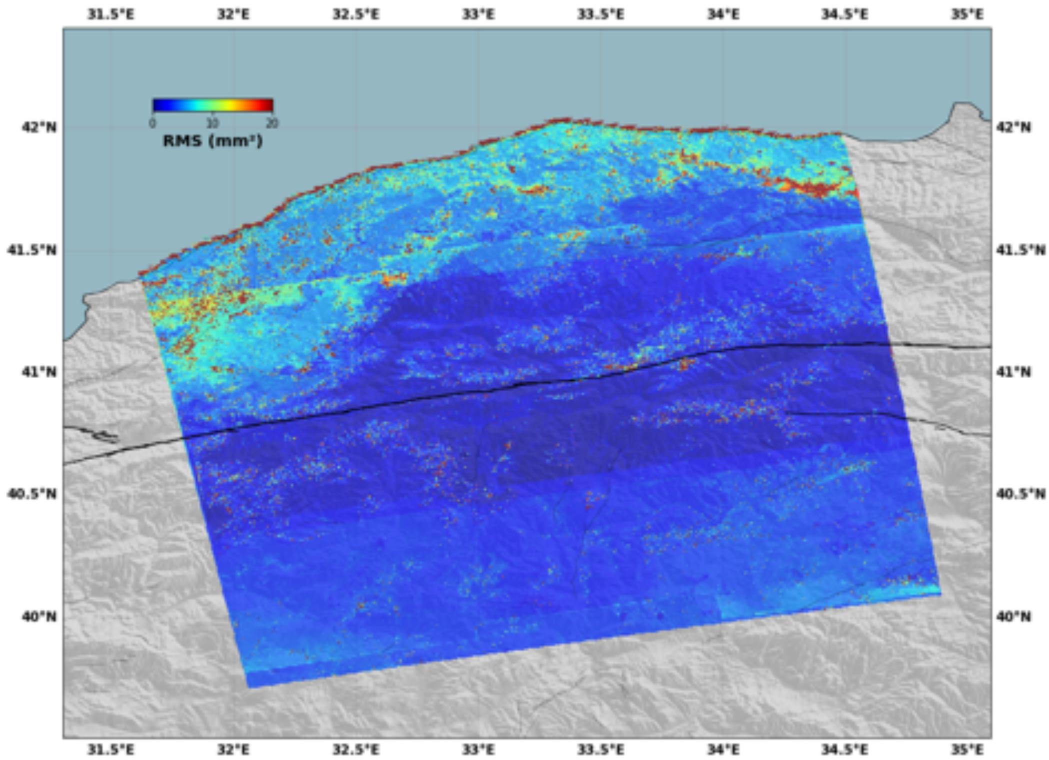


Figure S-14: **RMS of time series reconstruction for track 87 -** RMS is defined as the average of the square difference between data (i.e. interferograms) and time series reconstructions (i.e. interferograms predicted from the time series) and used as a quality factor for pixel selection.

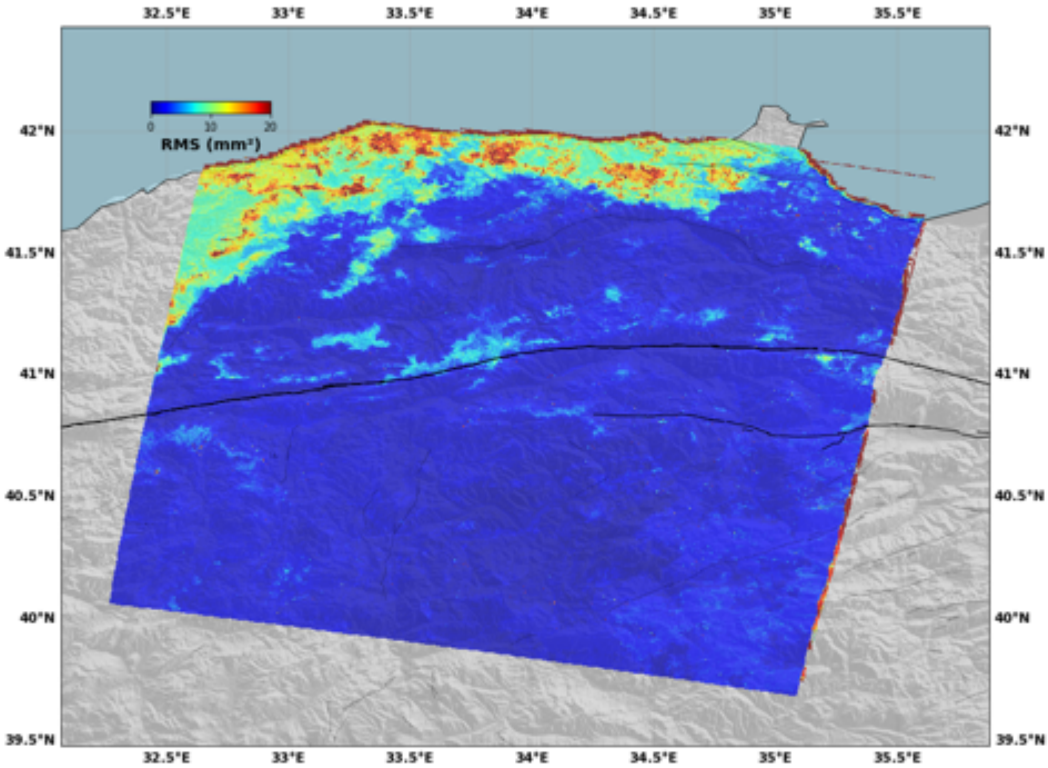


Figure S-15: **RMS of time series reconstruction for 167 -** RMS is defined as the average of the square difference between data (i.e. interferograms) and time series reconstructions (i.e. interferograms predicted from the time series) and used as a quality factor for pixel selection.

## 1.6 Additional results

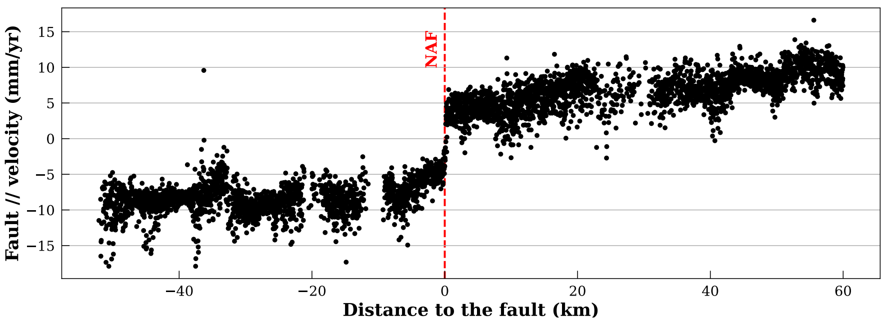


Figure S-16: **Fault perpendicular profile of fault parallel ground velocity -** This profile intersects the North Anatolian Fault in Ismetpasa.

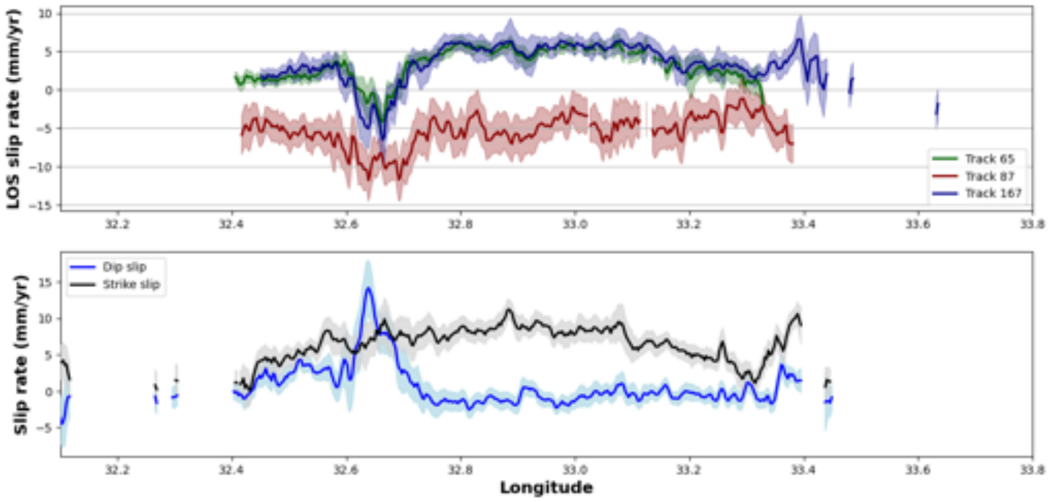


Figure S-17: **Along strike distribution of slip - Top** Along strike distribution of phase difference across the NAF in LOS for tracks 65 (green), 87 (red) and 167 (blue). Tracks 65 and 167 are both in the same geometry of acquisition (i.e. descending orbit), hence the remarkable agreement between the two independent datasets. Track 87 is along an ascending orbit. When motion is opposite on ascending and descending tracks LOS, ground motion is mostly horizontal as expected motion is aligned with the LOSs. When motion is opposite in LOS, ground motion is mostly vertical. **Bottom** Along strike distribution of horizontal and differential motion from the decomposition of the three tracks. As shown by the agreement between data shown above, ground motion is mostly horizontal (right lateral strike slip) along the fault with some vertical differential motion near Ismetpasa (northern block subsiding wrt. southern block).

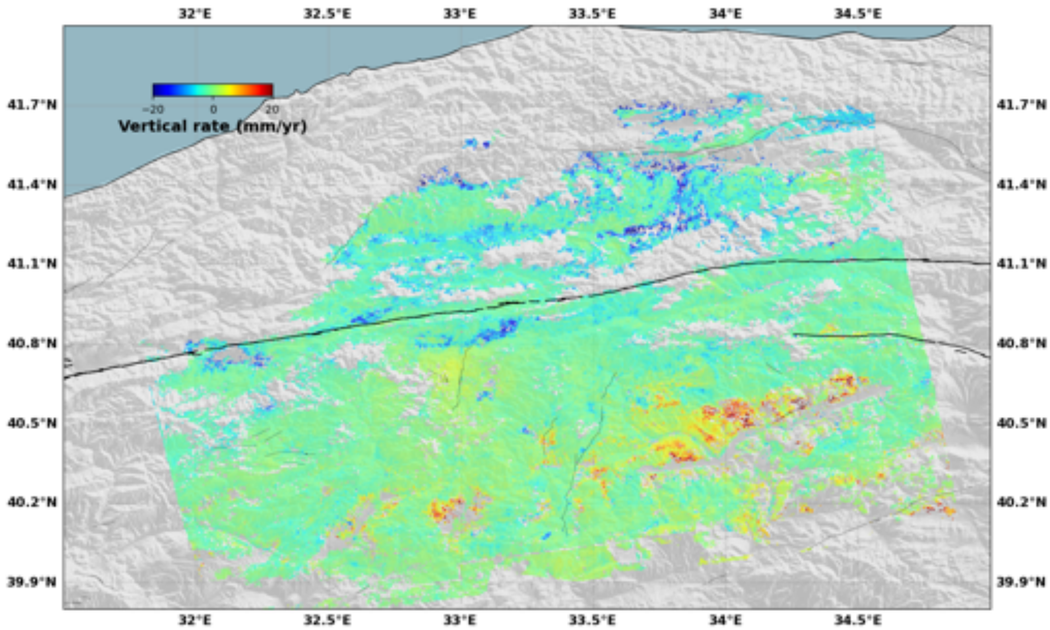


Figure S-18: **Map of vertical displacement rate -** This map results from the combination of the three velocity maps on track 65, 87 and 167.

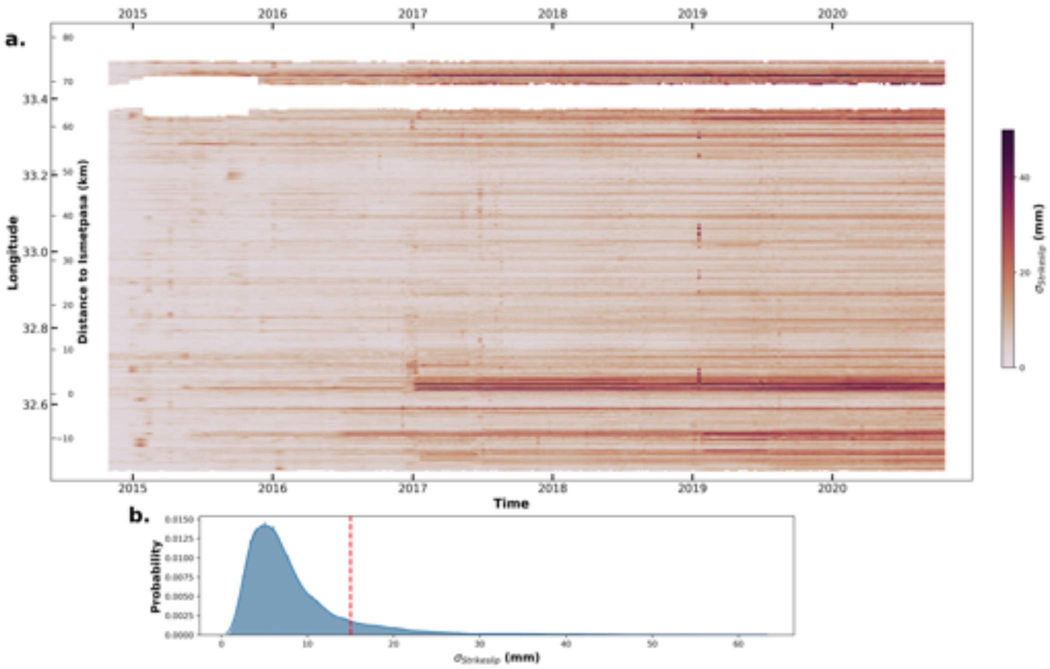


Figure S-19: **Uncertainties on strike slip motion -** Standard deviation of the strike slip motion as function of time. The uncertainty derives from the general least square inversion of the horizontal vs vertical relative motion between both sides of the fault. We consider the posterior covariance matrix and represent here the square root of the diagonal term. Bottom plot shows the distribution of these uncertainties with the threshold we have chosen for the representation in figure 4 of the main text.

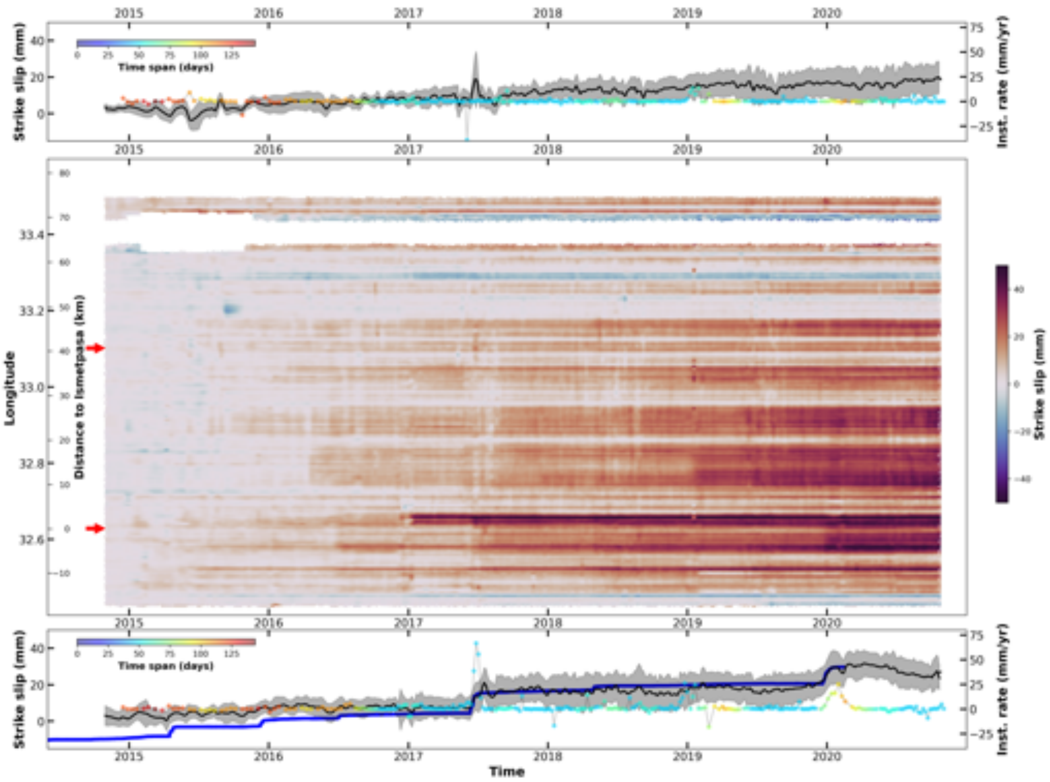


Figure S-20: **Time dependent surface slip rate -** Same as figure 4 of the main text without masking uncertain values.

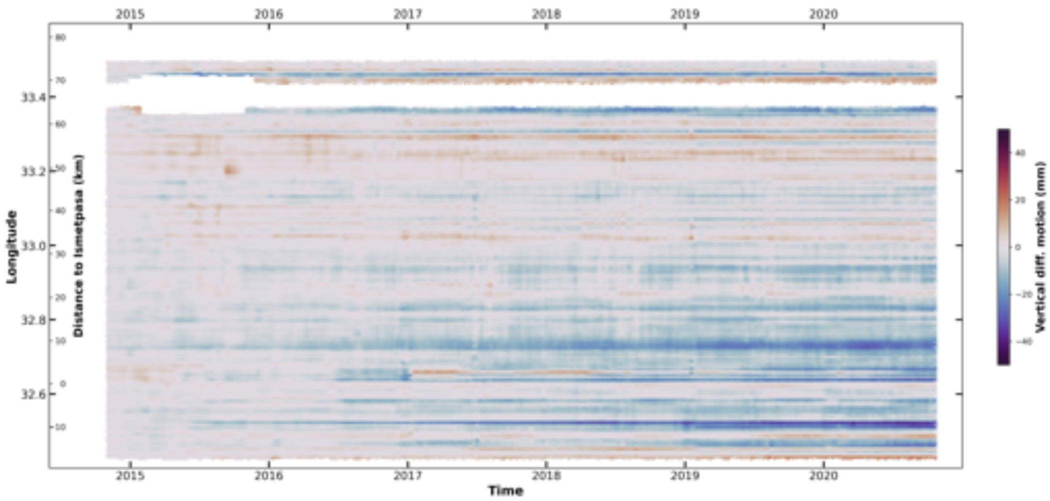


Figure S-21: **Time-dependent vertical differential motion -** Evolution of the vertical differential motion across the NAF. Blue indicates subsidence of the northern block wrt. the south.

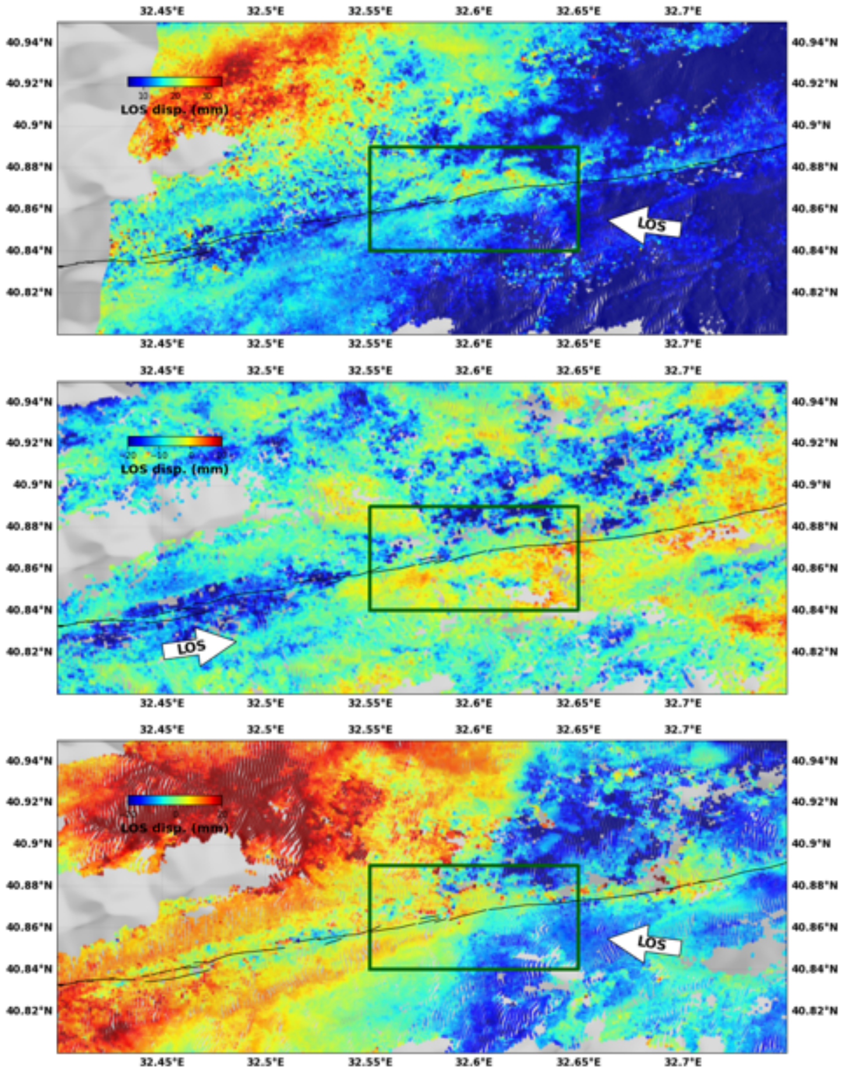


Figure S-22: **LOS displacement resulting from the slow slip event of 2017 -** Difference between time frames of the time series bracketing the slow slip event of 2017 from data on tracks 167 (top), 87 (center) and 65 (bottom). The white arrow indicates the direction from the satellite to the ground. Dark lines are fault traces. Dark rectangle indicates the region where the slow slip event is identified. The opposite sign of the across fault gradient between data on ascending and descending tracks confirms that motion is mainly horizontal.

## 2 GNSS dataset

We processed data from 77 continuous GNSS located in Eurasian (48 stations), Anatolian (21 stations), African (5 stations), Arabian (2 plates) and Somalia (1 station) Plates (Figure 1, a and b). We provide in table S-1 and S-2 the observation periods used in this paper and the measured velocities in the ITRF Eurasia-fixed reference frame, with our model predictions. Sites are grouped within the following networks:

- 8 GNSS from the International GNSS service, core network (`www.igs.org`): BHR4, CHUM, KIT3, MAT1, MDVJ, ONS1, POL2, RAMO, TASH
- 29 GNSS from the International GNSS service (`www.igs.org`): ADIS, ANKR, ARUC, BSHM, BUCU, CRAO, DJIG, DRAG, DYNG, GANP, GLSV, GRAZ, ISBA, ISTA, IZMI, KITG, KRS1, MERS, MIKL, NICO, ORID, PENC, POLV, SOFI, SULP, TEHN, TUBI, WARN, ZECK.
- 20 GNSS from the Turkish National Network (`https://www.tusaga-aktif.gov.tr/`): BOLU, BOL1, BOYT, CANK, CMLD, CORU, ESKS, HEND, HYMN, INE2, KKAL, KRBK, KSTM, KURU, NAHA, SIH1, SINP, SUNL, VEZI, ZONG.
- 19 GNSS from the ISMENET network: IS01, IS02, IS03, IS04, IS05, IS07, IS08, IS09, IS10, IS11, IS12, IS13, IS14, IS16, IS17, IS18, IS19, IS20, IS21. Each station of Ismenet includes a Zephyr geodetic antenna bolted in a boulder or custom made concrete monument and a NetR9 or NetRS receiver (Trimble) recording at 30 seconds, powered by either local power or solar panels. Antennas are covered by a radome.

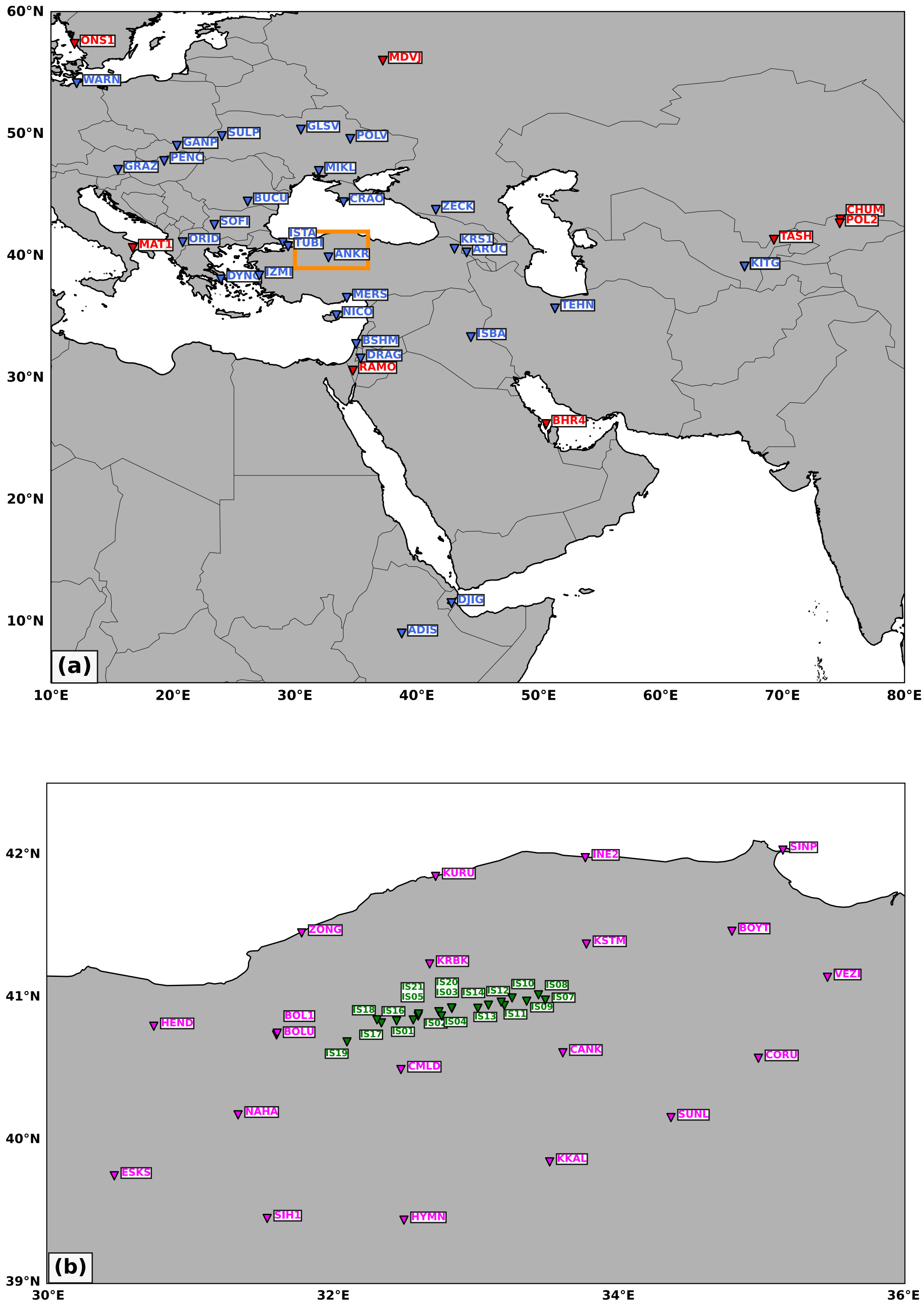


Figure S-23: **Selection of GNSS sites - a.** Extended selection including IGS, core network, sites (red) and IGS stations (blue). **b.** Local selection with sites from the Turkish Nation Network (pink) and from our ISMENET network (green).

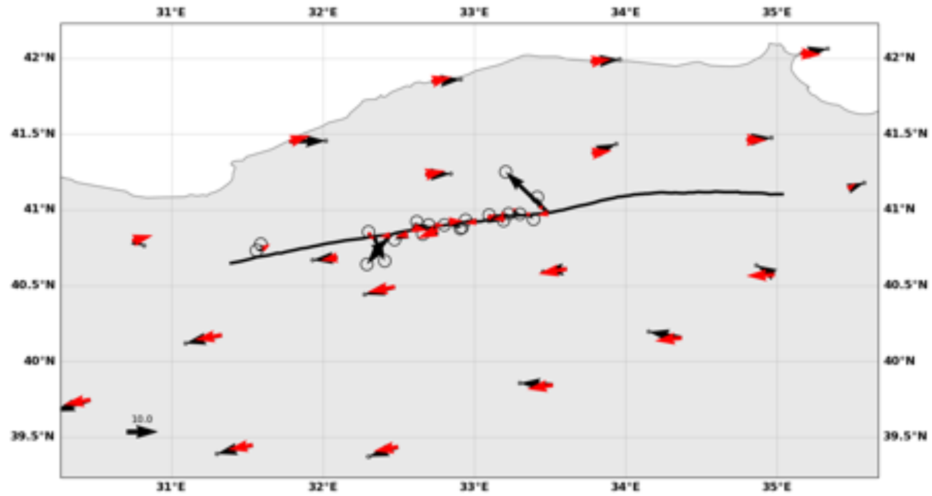


Figure S-24: **GNSS derived velocities and predictions from the mean model -** Map of the GNSS-derived velocities (black) together with the predictions from the mean model. Ellipses are 1-sigma. It is important to note that the mean model is not a model drawn from the posterior PDF, hence its predictions are not necessarily the best ones. In addition, error ellipses here only represent the formal uncertainties on the GNSS measurements feeding in $\mathbf{C}_d$ while our Bayesian approach assumes larger uncertainties deriving from the prediction error, $\mathbf{C}_p$.

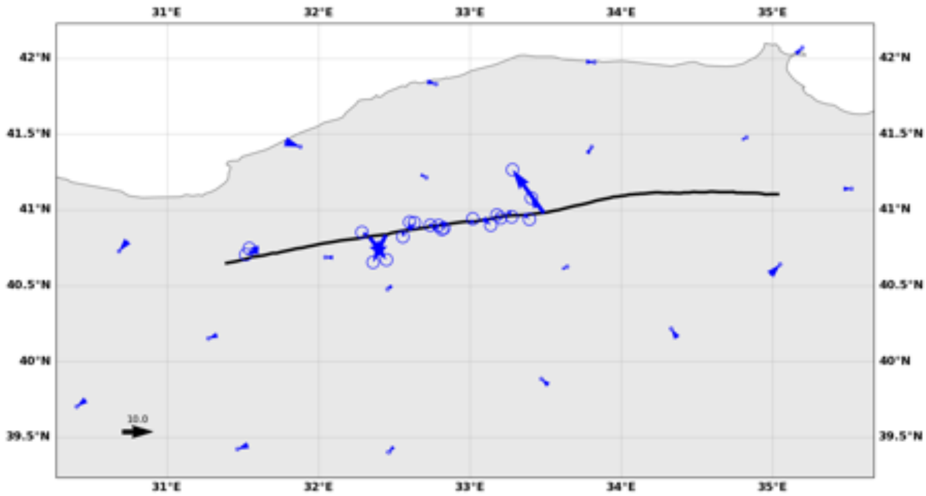


Figure S-25: **Residuals from the mean model -** Map of the residuals, as differences between velocities (black arrows on figure S-24) and predictions from the mean model (red arrows on figure S-24). Ellipses are 1-sigma. It is important to note that the mean model is not a model drawn from the posterior PDF, hence its predictions are not necessarily the best ones. In addition, error ellipses here only represent the formal uncertainties on the GNSS measurements feeding in $\mathbf{C}_d$ while our Bayesian approach assumes larger uncertainties deriving from the prediction error, $\mathbf{C}_p$.

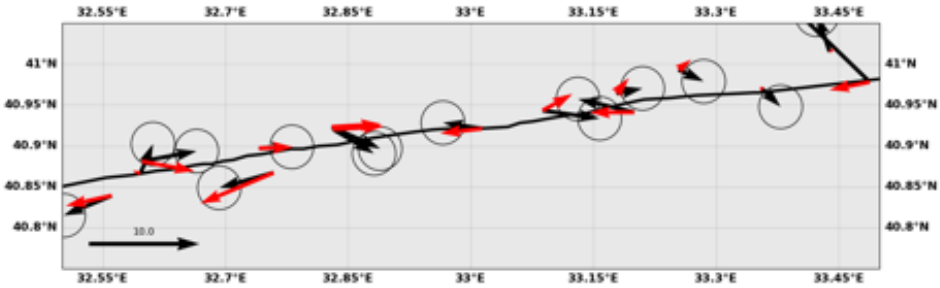


Figure S-26: **GNSS derived velocities and predictions from the mean model (close up) -** Map of the GNSS-derived velocities (black) together with the predictions from the mean model. Ellipses are 1-sigma. It is important to note that the mean model is not a model drawn from the posterior PDF, hence its predictions are not necessarily the best ones. In addition, error ellipses here only represent the formal uncertainties on the GNSS measurements feeding in $\mathbf{C}_d$ while our Bayesian approach assumes larger uncertainties deriving from the prediction error, $\mathbf{C}_p$.

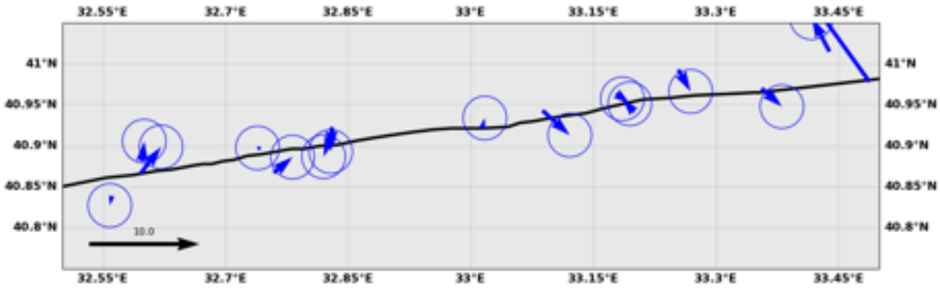


Figure S-27: **Residuals from the mean model (close up)-** Map of the residuals, as differences between velocities (black arrows on figure S-24) and predictions from the mean model (red arrows on figure S-24). Ellipses are 1-sigma. It is important to note that the mean model is not a model drawn from the posterior PDF, hence its predictions are not necessarily the best ones. In addition, error ellipses here only represent the formal uncertainties on the GNSS measurements feeding in $\mathbf{C}_d$ while our Bayesian approach assumes larger uncertainties deriving from the prediction error, $\mathbf{C}_p$.

| NAME | Lon ($^o$) | Lat ($^o$) | First Obs (dec year) | Last Obs (dec year) |
|---|---|---|---|---|
| BOL1 | 31.606 | 40.746 | 2018.884 | 2021.578 |
| BOLU | 31.602 | 40.734 | 2016.534 | 2018.774 |
| BOYT | 34.797 | 41.461 | 2016.534 | 2021.578 |
| CANK | 33.610 | 40.609 | 2016.534 | 2021.578 |
| CMLD | 32.475 | 40.491 | 2016.534 | 2021.578 |
| CORU | 34.982 | 40.570 | 2016.534 | 2021.578 |
| ESKS | 30.464 | 39.746 | 2016.534 | 2021.578 |
| HEND | 30.741 | 40.795 | 2016.534 | 2021.578 |
| HYMN | 32.496 | 39.435 | 2016.534 | 2020.750 |
| INE2 | 33.768 | 41.977 | 2016.534 | 2020.127 |
| KKAL | 33.518 | 39.843 | 2016.534 | 2021.578 |
| KRBK | 32.676 | 41.232 | 2016.534 | 2021.578 |
| KSTM | 33.776 | 41.371 | 2016.534 | 2021.578 |
| KURU | 32.718 | 41.846 | 2016.534 | 2021.578 |
| NAHA | 31.332 | 40.173 | 2016.534 | 2021.578 |
| SIH1 | 31.536 | 39.447 | 2016.534 | 2021.578 |
| SINP | 35.154 | 42.030 | 2016.534 | 2021.578 |
| SUNL | 34.369 | 40.154 | 2016.534 | 2020.059 |
| VEZI | 35.467 | 41.138 | 2016.534 | 2021.578 |
| ZONG | 31.778 | 41.450 | 2016.534 | 2021.578 |
| IS01 | 32.561 | 40.839 | 2016.537 | 2021.578 |
| IS02 | 32.741 | 40.897 | 2016.534 | 2021.578 |
| IS03 | 32.832 | 40.920 | 2016.534 | 2019.453 |
| IS04 | 32.759 | 40.867 | 2016.542 | 2021.578 |
| IS05 | 32.596 | 40.866 | 2016.944 | 2019.448 |
| IS07 | 33.488 | 40.978 | 2019.456 | 2021.578 |
| IS08 | 33.439 | 41.015 | 2019.456 | 2021.578 |
| IS09 | 33.356 | 40.970 | 2019.456 | 2021.578 |
| IS10 | 33.254 | 40.993 | 2019.456 | 2021.578 |
| IS11 | 33.200 | 40.941 | 2019.440 | 2021.578 |
| IS12 | 33.178 | 40.964 | 2019.440 | 2021.578 |

| | | | | |
|---|---|---|---|---|
| IS13 | 33.088 | 40.943 | 2019.462 | 2021.578 |
| IS14 | 33.014 | 40.921 | 2019.442 | 2021.578 |
| IS16 | 32.444 | 40.833 | 2019.451 | 2021.578 |
| IS17 | 32.338 | 40.818 | 2019.451 | 2021.578 |
| IS18 | 32.307 | 40.840 | 2019.445 | 2021.578 |
| IS19 | 32.096 | 40.685 | 2019.445 | 2021.578 |
| IS20 | 32.830 | 40.923 | 2019.456 | 2021.578 |
| IS21 | 32.598 | 40.881 | 2019.451 | 2021.578 |

Table S-1: **GNSS observation period -** Period of observation for the stations used in this study. Sites with names starting with IS have been installed over the duration of the Geo4D project.

| **Site** | **Lon** | **Lat** | **Data** | | **Ref. removed** | | **Model** | |
|---|---|---|---|---|---|---|---|---|
| | | | East | North | East | North | East | North |
| | (°E) | (°N) | (mm/yr) | | (mm/yr) | | (mm/yr) | |
| BOL1 | 31.606 | 40.746 | -11.288 | 1.658 | -0.812 | 1.364 | 2.333 | 1.425 |
| BOLU | 31.602 | 40.734 | -12.533 | 0.150 | -2.058 | -0.144 | 2.032 | 1.375 |
| BOYT | 34.797 | 41.461 | -2.306 | 1.212 | 8.235 | 0.699 | 6.768 | -0.107 |
| CANK | 33.610 | 40.609 | -18.258 | -0.437 | -7.795 | -0.869 | -9.410 | -1.626 |
| CMLD | 32.475 | 40.491 | -20.448 | -2.175 | -9.996 | -2.529 | -9.063 | -1.735 |
| CORU | 34.982 | 40.570 | -16.440 | 3.662 | -5.979 | 3.135 | -9.325 | -0.321 |
| ESKS | 30.464 | 39.746 | -22.154 | -3.658 | -11.767 | -3.871 | -8.779 | -1.599 |
| HEND | 30.741 | 40.795 | -6.565 | -1.383 | 3.917 | -1.617 | 6.812 | 1.830 |
| HYMN | 32.496 | 39.435 | -20.045 | -2.878 | -9.689 | -3.233 | -8.104 | -1.467 |
| INE2 | 33.768 | 41.977 | -0.994 | 1.224 | 9.593 | 0.782 | 6.868 | 0.897 |
| KKAL | 33.518 | 39.843 | -21.268 | 1.046 | -10.875 | 0.620 | -8.596 | -1.381 |
| KRBK | 32.676 | 41.232 | -2.085 | 0.631 | 8.434 | 0.263 | 6.625 | 1.256 |
| KSTM | 33.776 | 41.371 | -2.482 | 3.587 | 8.050 | 3.144 | 6.638 | 0.991 |
| KURU | 32.718 | 41.846 | -0.953 | 1.058 | 9.622 | 0.687 | 6.695 | 1.539 |
| NAHA | 31.332 | 40.173 | -22.371 | -2.478 | -11.947 | -2.752 | -9.020 | -1.634 |

| | | | | | | | | |
|---|---|---|---|---|---|---|---|---|
| SIH1 | 31.536 | 39.447 | -22.170 | -2.629 | -11.812 | -2.916 | -8.289 | -1.555 |
| SINP | 35.154 | 42.030 | -1.619 | 2.183 | 8.974 | 1.647 | 6.933 | -0.319 |
| SUNL | 34.369 | 40.154 | -21.295 | 2.540 | -10.873 | 2.055 | -8.906 | -0.973 |
| VEZI | 35.467 | 41.138 | -5.164 | 2.521 | 5.349 | 1.962 | 2.693 | 1.947 |
| ZONG | 31.778 | 41.450 | 1.545 | 0.546 | 12.085 | 0.239 | 6.955 | 1.976 |
| IS01 | 32.561 | 40.839 | -14.892 | -1.461 | -4.408 | -1.821 | -4.220 | -0.934 |
| IS02 | 32.741 | 40.897 | -7.470 | 0.490 | 3.019 | 0.118 | 3.148 | 0.093 |
| IS03 | 32.832 | 40.920 | -6.757 | -1.834 | 3.734 | -2.213 | 4.631 | 0.287 |
| IS04 | 32.759 | 40.867 | -15.465 | -1.008 | -4.979 | -1.382 | -6.709 | -2.817 |
| IS05 | 32.596 | 40.866 | -9.314 | 3.076 | 1.172 | 2.714 | -0.715 | 0.274 |
| IS07 | 33.488 | 40.978 | -24.545 | 14.010 | -14.049 | 13.586 | -3.717 | -0.733 |
| IS08 | 33.439 | 41.015 | -11.663 | 3.820 | -1.163 | 3.400 | 0.474 | 0.301 |
| IS09 | 33.356 | 40.970 | -8.766 | -1.259 | 1.729 | -1.674 | -0.133 | -0.016 |
| IS10 | 33.254 | 40.993 | -8.176 | -0.664 | 2.322 | -1.072 | 1.187 | 0.932 |
| IS11 | 33.200 | 40.941 | -15.648 | 1.616 | -5.155 | 1.212 | -4.080 | -0.014 |
| IS12 | 33.178 | 40.964 | -8.079 | 0.865 | 2.416 | 0.463 | 1.159 | 1.418 |
| IS13 | 33.088 | 40.943 | -5.261 | -0.326 | 5.232 | -0.722 | 2.739 | 1.534 |
| IS14 | 33.014 | 40.921 | -14.088 | 0.928 | -3.597 | 0.537 | -3.850 | -0.429 |
| IS16 | 32.444 | 40.833 | -18.174 | -9.313 | -7.691 | -9.665 | -3.527 | -0.675 |
| IS17 | 32.338 | 40.818 | -6.993 | -7.463 | 3.489 | -7.807 | -2.052 | -0.390 |
| IS18 | 32.307 | 40.840 | -10.802 | 1.037 | -0.318 | 0.695 | 0.673 | 0.148 |
| IS19 | 32.096 | 40.685 | -18.671 | -0.552 | -8.201 | -0.880 | -5.683 | -0.940 |
| IS20 | 32.830 | 40.923 | -6.038 | -1.609 | 4.453 | -1.987 | 4.545 | 0.266 |
| IS21 | 32.598 | 40.881 | -5.467 | 1.295 | 5.020 | 0.933 | 4.823 | -0.910 |

Table S-2: **GNSS data, corrected data and model -** Table of GNSS rates used in this article. Data refers to the original GNSS velocities in the Eurasia-fixed referenced frame. Ref. removed refers to the original velocities corrected from the translation and rotation term inferred in the inversion procedure. Model refers to the displacement rates predicted by the slip model. Sites with names starting with IS have been installed over the duration of the Geo4D project.

## 3 Model additional information and performance

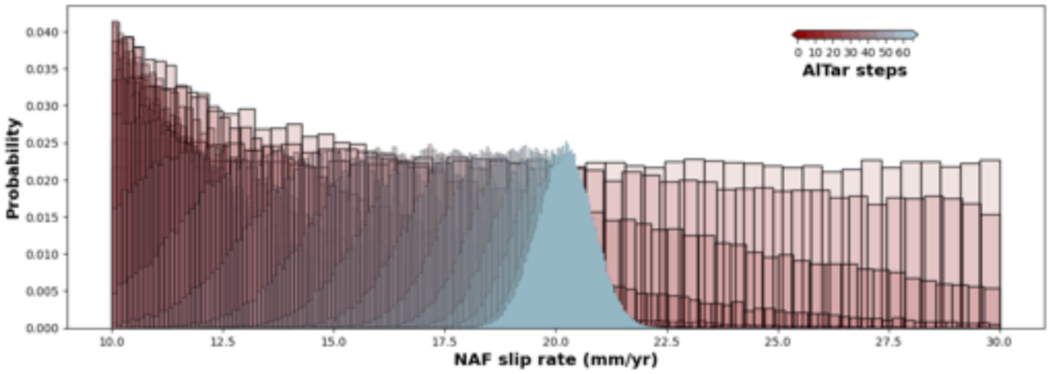


Figure S-28: **Example of convergence during tempering -** While the sampler marches forward, it progressively shrinks the sample set onto the final, posterior PDF. Here, we show the marginal PDF of the deep slip rate on the NAF, which transitions at each step from the a priori uniform distribution to the posterior, which, in this case, is a Gaussian distribution.

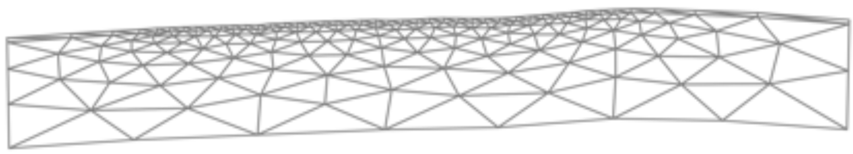

Figure S-29: **Triangular mesh for the shallow part of the NAF -** 3D representation of the triangular mesh used for the shallow section of the NAF. Shallowest triangles are 1 km-sized while largest, deepest ones are  10 km-size. Shallowest row intersects the surface while deepest row reaches 20 km.

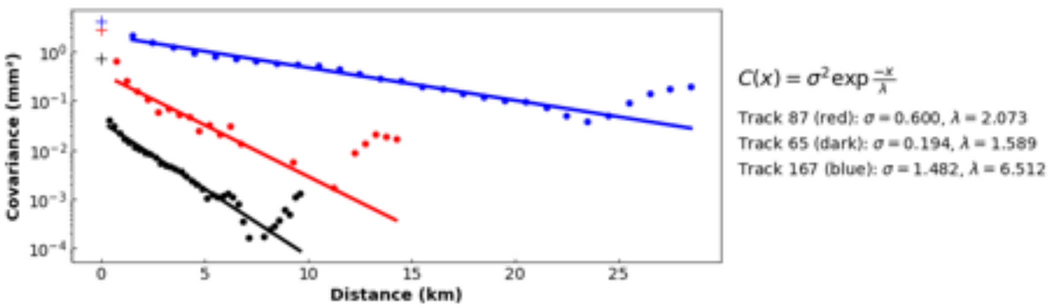


Figure S-30: **Covariance functions for the InSAR velocity maps -** Empirical covariances of the velocity maps from tracks 65 (dark), 87 (red) and 167 (red). Dots are the empirical covariances. Lines are the exponential fit to the covariance functions. Crosses are the variance of the data (auto-correlation).

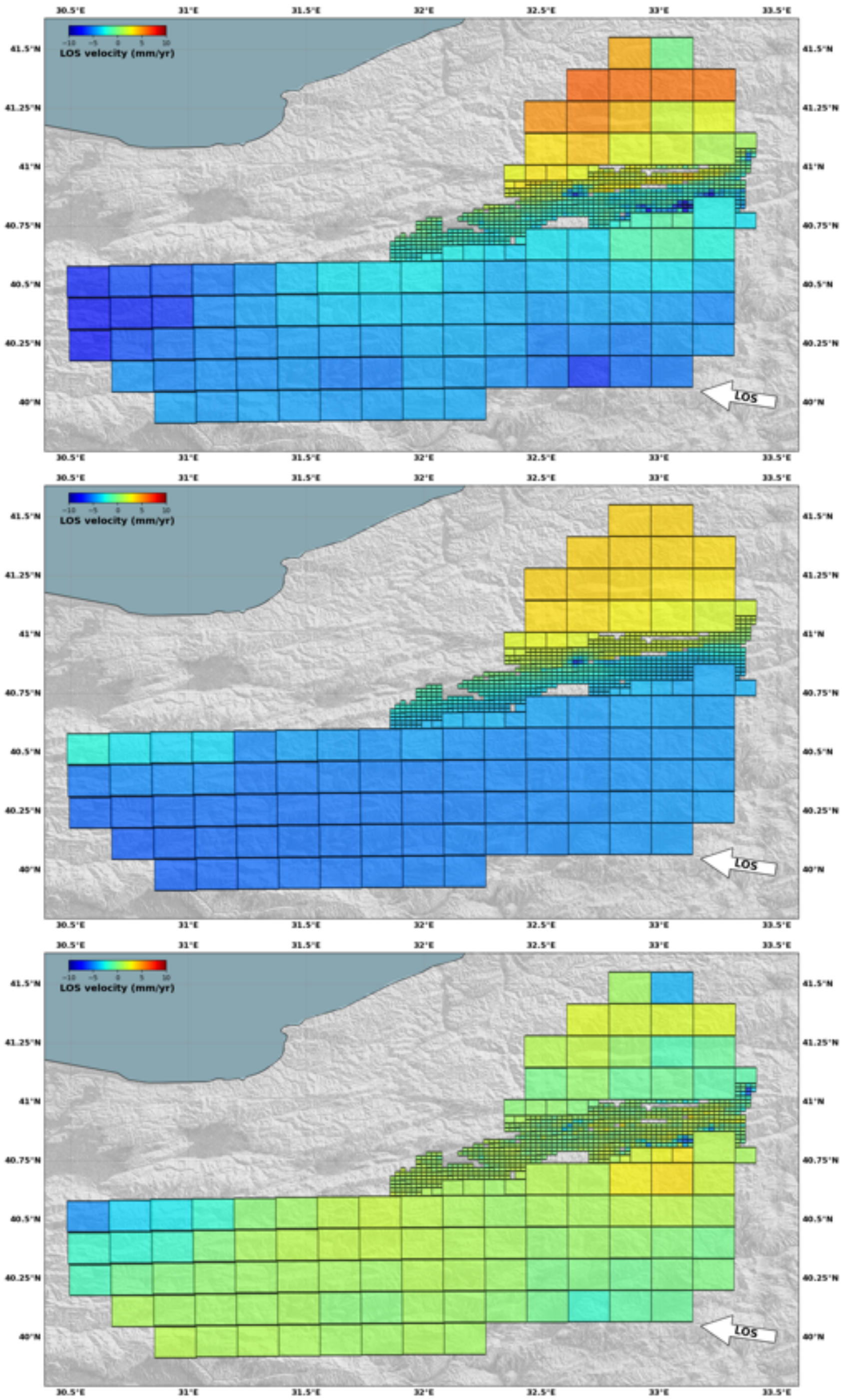


Figure S-31: **Decimated velocity field from track 65 -** Decimation geometry and resulting input data set for the slip rate inversion (top), prediction from the mean model (center) and residuals (bottom).

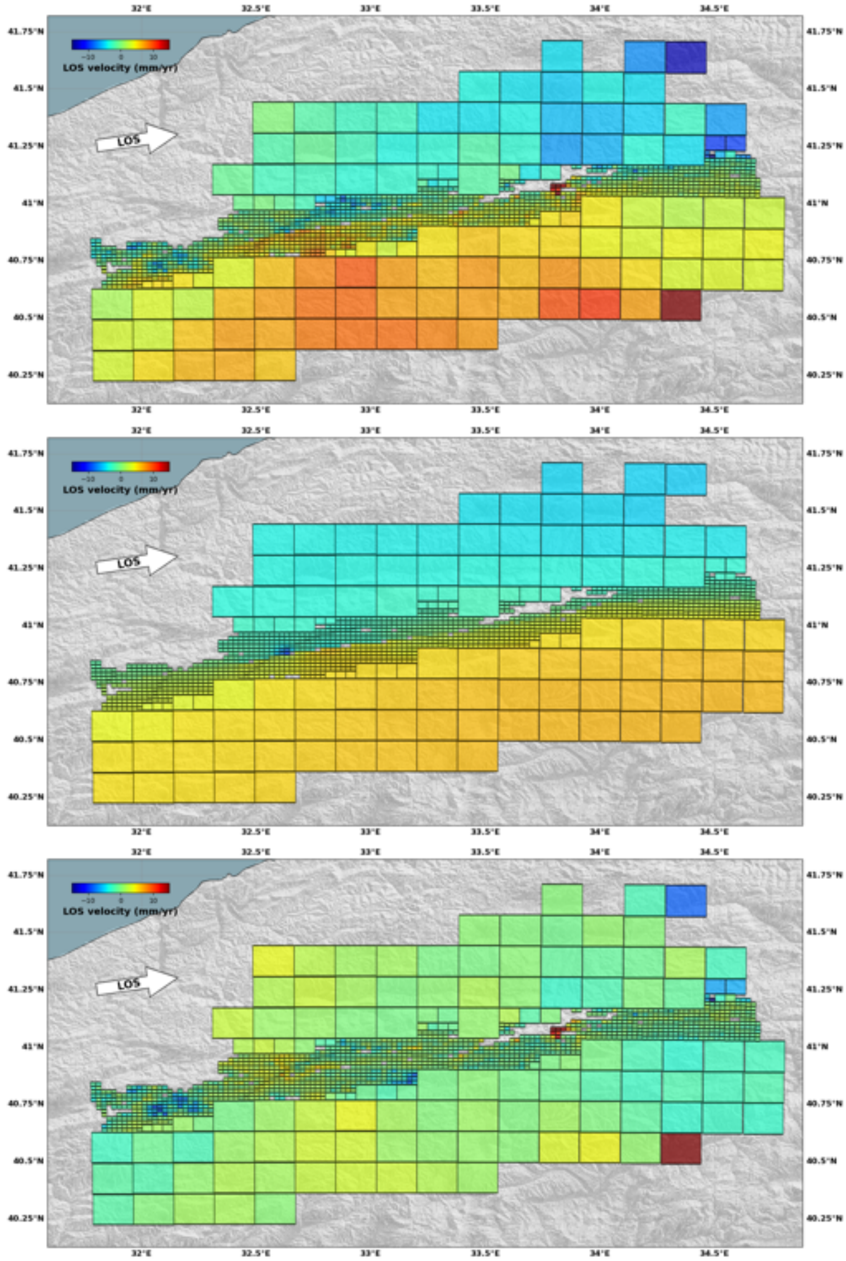


Figure S-32: **Decimated velocity field from track 87 -** Decimation geometry and resulting input data set for the slip rate inversion (top), prediction from the mean model (center) and residuals (bottom).

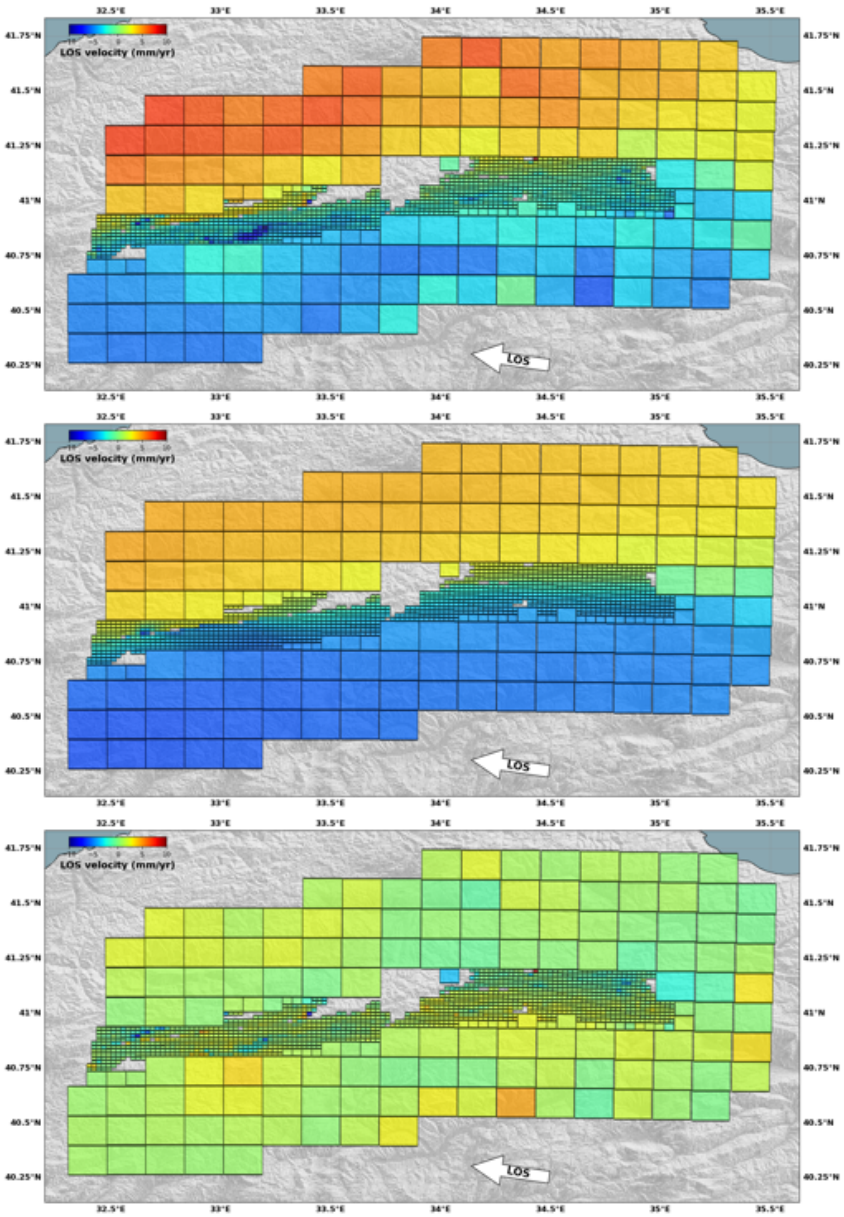


Figure S-33: **Decimated velocity field from track 167 -** Decimation geometry and resulting input data set for the slip rate inversion (top), prediction from the mean model (center) and residuals (bottom).

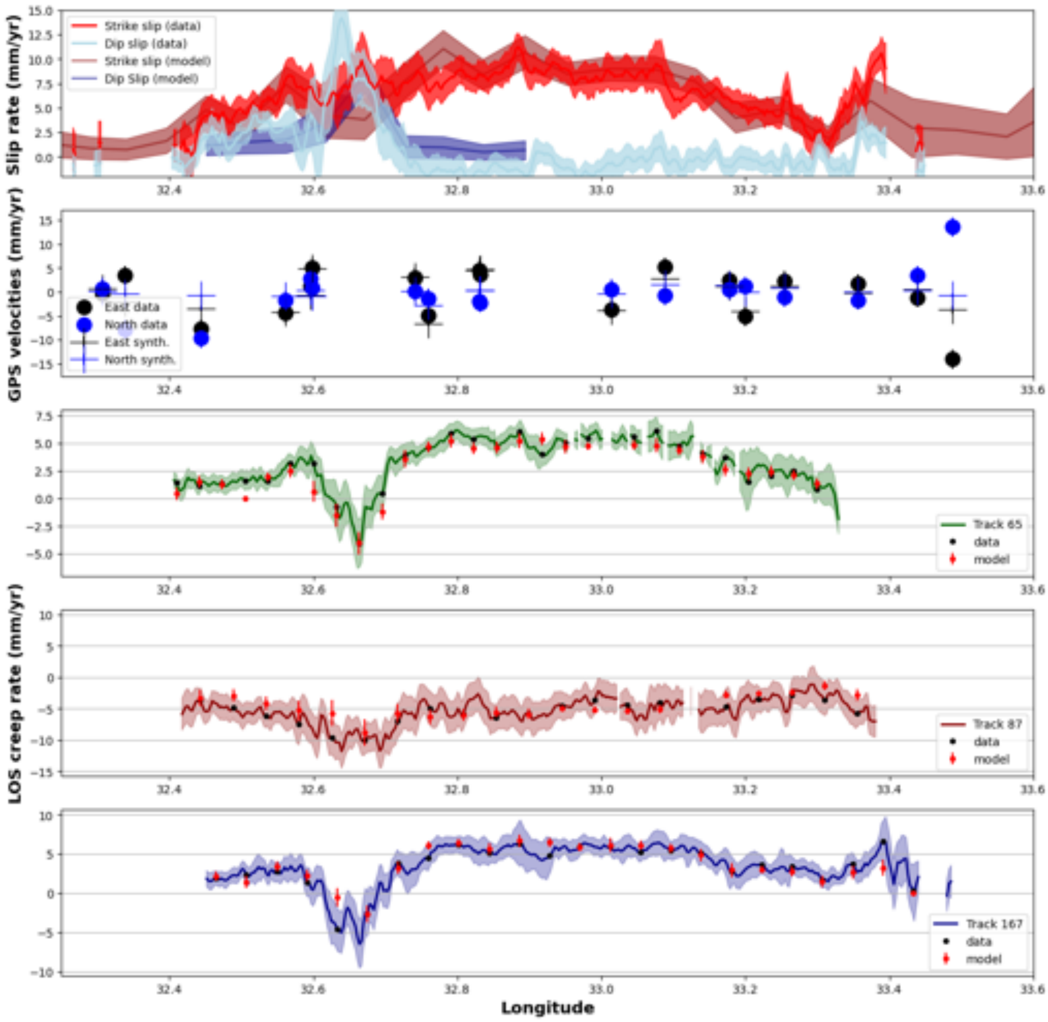


Figure S-34: **Fit to the surface fault slip data - Top** Surface slip rate measured on the horizontal and vertical ground motion maps and surface slip rate from the posterior PDF of the slip rate model. Red is for strike slip and blue for vertical differential motion (i.e. dip slip). **Second** Data (circles) and predictions from the mean model (crosses) for the GNSS data along the fault in the east (black) and north (blue) directions. **Three bottom plots** Data (lines) and predictions from the mean model for the surface slip measured on InSAR velocity maps.

## 4 Slip rates at Ismetpasa

All slip rates from table S-3 were measured within a short distance from the city of Ismetpasa. Most of these measurements were made within the city, at the train station, while some of them average over a distance difficult to estimate, depending on the publication. Refer to Bilham et al. (2016) for a detailed description of these surface slip rates. Rates are from Ambraseys (1970), Aytun (1982), Eren (1984), Deniz et al. (1993), Altay and Sav (1991), Çakir et al. (2005), Kutoglu and Akcin (2006), Kutoglu et al. (2008), Kutoglu et al. (2010), Karabacak et al. (2011), Deguchi (2011), Ozener et al. (2013) and Kaneko et al. (2012). Some rates were re-evaluated by Bilham et al. (2016). We have manually digitized figure 5 of Altay and Sav (1991).

| **Time** | **Creep rate mm/yr** | **Std dev mm/yr** | **Observation Period start - end** | **Source** | **Measurement type** |
|---|---|---|---|---|---|
| 1963 | 10.40 | 0.40 | 1957-1969 | Ambraseys (1970) | Wall offset (photo) |
| 1975 | 10.80 | 0.40 | 1969-1979 | Aytun (1982) | Triangulation |
| 1977 | 10.20 | 0.60 | 1972-1979 | Eren (1984) | Trilateration |
| 1987 | 9.30 | 0.70 | 1982-1992 | Deniz et al. (1993) | Trilateration |
| 1997 | 7.80 | 0.50 | 1992-2002 | Kutoglu and Akcin (2006) | GNSS |
| 1986 | 7.30 | 0.10 | 1982-1990 | Altay and Sav (1991) | Creepmeter |
| 2004 | 12.00 | 1.30 | 2002-2007 | Kutoglu et al. (2008) | GNSS |
| 2007 | 15.10 | 4.10 | 2007-2008 | Kutoglu et al. (2010) | GNSS |
| 1996 | 8.00 | 3.00 | 1992-2001 | Çakir et al. (2005) | InSAR |
| 2008 | 8.35 | 0.24 | 2003-2011 | Cetin et al. (2014) | InSAR |
| 2009 | 8.40 | 1.60 | 2007-2009 | Karabacak et al. (2011) | LiDAR |
| 2008 | 7.60 | 1.10 | 2005-2011 | Ozener et al. (2013) | GNSS |
| 2009 | 9.00 | 1.00 | 2007-2011 | Kaneko et al. (2013) | InSAR |
| 1992 | 8.30 | 0.10 | 1969-2016 | Bilham et al. (2016) | Wall offset |
| 1999 | 7.10 | 0.30 | 1984-2016 | Bilham et al. (2016) | Wall offset |
| 1976 | 9.90 | 0.30 | 1969-1984 | Bilham et al. (2016) | Wall offset (photo) |
| 2015 | 5.90 | 0.10 | 2014-2016 | Bilham et al. (2016) | Creepmeter |
| 2015 | 6.10 | 1.00 | 2014-2016 | Bilham et al. (2016) | Wall offset |
| 2017 | 6.00 | 2.00 | 2014-2021 | This study | S1 InSAR |

Table S-3: **Slip rates at Ismetpasa -** Table of slip rates measured at Ismetpasa since the 1950's. Please be aware that this table is almost entirely a copy of that from Bilham et al 2016 and this paper should be cited whenever this table is used.

## References


Altay, C., & Sav, H. (1991). Continuous creep measurement along the North Anatolian Fault zone. *Bulletin of the geological congres of Turkey*, *6*, 77–84.

Ambraseys, N. N. (1970). Some characteristic features of the Anatolian fault zone. *Tectonophysics*, *9*, 143–165.

Aytun, A. (1982). Creep Measurements in the Ismetpaşa Region of the North Anatolian Fault Zone. *Multidisciplinary Approach to Earthquake Prediction Progress in Earthquake Prediction Research*, *2*, 279–292.

Bilham, R., Ozener, H., Mencin, D., Dogru, A., ERGINTAV, S., CAKIR, Z., ... Mattioli, G. (2016). Surface creep on the North Anatolian Fault at Ismetpasa, Turkey, 1944-2016. *Journal of Geophysical Research-Solid Earth*, *121*, 7409–7431. doi: 10.1002/2016JB013394

Çakir, Z., Akoglu, A., Belabbes, S., Ergintav, S., & Meghraoui, M. (2005). Creeping along the Ismetpasa section of the North Anatolian fault (Western Turkey): Rate and extent from InSAR. *Earth and Planetary Science Letters*, *238*(1-2), 225–234. doi: 10.1016/j.epsl.2005.06.044

Deguchi. (2011). Detection of fault creep around naf by insar time series analysis using palsar data. *Proc. of SPIE, SAR Image Analysis, Modeling, and Techniques XI*, *8179*. doi: 10.1117/12.898478

Deniz, R., Aksoy, A., Yalin, D., Seeger, H., Franke, P., Hirsch, O., & Bautsch, P. (1993). Determination of crustal movements in turkey by terrestrial geodetic methods. *Journal of Geodynamics*, *18*(1), 13–22. doi: https://doi.org/10.1016/0264-3707(93)90024-Z

Eren, K. (1984). Strain analysis along the north analtolian fault by using geodetic surveys. *Bulletin géodésique*, *58*(2), 137–150. doi: 10.1007/BF02520898

Kaneko, Y., Fialko, Y., Sandwell, D. T., Tong, X., & Furuya, M. (2012). Interseismic deformation and creep along the central section of the North Anatolian fault (Turkey): InSAR observations and implications for rate-and-state friction properties. *Journal of Geophysical Research-Solid Earth*, *118*, 316– 331. doi: 10.1029/2012JB009661

Karabacak, V., Altunel, E., & Cakir, Z. (2011). Monitoring aseismic surface creep along the north anatolian fault (turkey) using ground-based lidar. *Earth and Planetary Science Letters*, *304*(1), 64–70. doi: 10.1016/j.epsl.2011.01.017

Kutoglu, H. S., & Akcin, H. (2006). Determination of the 30-year creep trend on the ismetpaşa segment of the north anatolian fault using an old geodetic network. *Earth, Planets and Space*, *58*(8), 937–942. doi: 10.1186/BF03352598

Kutoglu, H. S., Akcin, H., Gundogdu, O., Gormus, K. S., & Koksal, E. (2010, 12). Relaxation on the ismetpasa segment of the north anatolian fault after the golcuk $m_w = 7.4$ and duzce $m_w = 7.2$ shocks. *Nat. Hazards Earth Syst. Sci.*, *10*(12), 2653–2657. doi: 10.5194/nhess-10-2653-2010

Kutoglu, H. S., Akcin, H., Kemaldere, H., & Gormus, K. S. (2008, 12). Triggered creep rate on the ismetpasa segment of the north anatolian fault. *Nat. Hazards Earth Syst. Sci.*, *8*(6), 1369–1373. doi: 10.5194/nhess-8-1369-2008

Ozener, H., Dogru, A., & Turgut, B. (2013). Quantifying aseismic creep on the ismetpasa segment of the north anatolian fault zone (turkey) by 6 years of gps observations. *Journal of Geodynamics*, *67*, 72–77. doi: 10.1016/j.jog.2012.08.002